CMS Draft Analysis Note

The content of this note is intended for CMS internal use and distribution only

2013/09/19
Head Id: 206780
Archive Id: 207516M
Archive Date: 2013/09/12
Archive Tag: trunk

Angular coefficients measurements in DY events

Matthew Jones[1], David Silvers[1], Arie Bodek[2], Jiyeon Han[2??]

[1] Purdue University
[2] University of Rochester

Abstract

We report on the first measurement of the angular distributions of final state lepton in $pp \to \gamma^*/Z \to \mu^+\mu^-$ events produced in the Z boson mass region ($80 < M_{ee} < 100$ GeV/c^2) at $\sqrt{s} = 7$ TeV. The data sample collected by the CMS detector corresponds to 4.9 fb^{-1} of integrated luminosity. The transverse momentum dependence of angular coefficients A_0, A_1, A_2, A_3, and A_4 are compared with POWHEG Monte Carlo generators based on Quantum Chromodynamics (QCD). The transverse momentum dependence of A_0 is in agreement with the predictions of perturbative QCD, but A_2 is lower than the prediction at large transverse momentum proceeds via a combination of the quark-antiquark annihilation and the quark-gluon Compton processes.

1 Introduction

The angular distribution of the final state muon in the quark-antiquark ($q\bar{q}$) annihilation process $q\bar{q} \rightarrow \gamma^*/Z \rightarrow \mu^+\mu^-$ can be written as

$$\frac{d\sigma}{dcos\theta} \quad \propto \quad (1 + cos^2\theta) + B\ cos\theta.$$

When quarks are bound in a nucleon (e.g. $pp \rightarrow \gamma^*/Z \rightarrow \mu^+\mu^-\ X$), the γ^*/Z is in general produced with a finite transverse momentum. In Quantum Chromodynamics (QCD) at leading order (LO) this occurs either through the annihilation process with a gluon (g) in the final state ($q\bar{q} \rightarrow \gamma^*/Z\ g$), or via the Compton process with a quark in the final state ($qg \rightarrow \gamma^*/Z\ q$), as shown in figure 1. The general expression[1] for angular distribution of the final state electron in the Collins-Soper(CS) frame[2] is given by:

$$\begin{aligned}\frac{d\sigma}{d\cos\theta d\phi} \quad &\propto \quad (1+\cos^2\theta) + \frac{1}{2}A_0(1-3\cos^2\theta) + A_1\sin 2\theta\cos\phi + \frac{1}{2}A_2\sin^2\theta\cos 2\phi \\ &+ \quad A_3\sin\theta\cos\phi + A_4\cos\theta + A_5\sin^2\theta\sin 2\phi + A_6\sin 2\theta\sin\phi + A_7\sin\theta\sin\phi.\end{aligned}$$

Here, θ and ϕ are the polar and azimuthal angles of the muon in the CS frame. The angular coefficients $A_0 - A_7$ are in general functions of the invariant mass $M_{\ell\ell}$, rapidity y, and transverse momentum P_T of the dilepton in the lab frame[3].

When integrated over ϕ the differential cross section reduces to:

$$\frac{d\sigma}{d\cos\theta} \propto (1+\cos^2\theta) + \frac{1}{2}A_0(1-3\cos^2\theta) + A_4\cos\theta \tag{1}$$

When integrated over $cos\theta$, the differential cross section reduces to:

$$\begin{aligned}\frac{d\sigma}{d\phi} &\propto 1 + \beta_3\cos\phi + \beta_2\cos 2\phi + \beta_7\sin\phi + \beta_5\sin 2\phi \qquad (2)\\ \beta_3 &= \frac{3\pi A_3}{16},\ \beta_2 = \frac{A_2}{4}, \beta_7 = \frac{3\pi A_7}{16},\ \beta_5 = \frac{A_5}{4}.\end{aligned}$$

The A_1 and A_6 terms vanish when the differential cross section is integrated over $\cos\theta$, or ϕ, respectively.

Calculations which are based on perturbative QCD (pQCD) make definite predictions for all of the angular coefficients. For $pp \rightarrow \gamma^*/Z \rightarrow \mu^+\mu^-\ X$ the angular coefficients A_5, A_6 and A_7 are close to zero [1], and if we integrate over positive and negative y, the angular coefficients A_1 and A_3 are small. We can use equation 1 to extract A_0 and A_4 and equation 3 to extract A_2 and A_3 under the assumption that A_5 and A_7 are zero (as is theoretically expected).

For the $q\bar{q} \rightarrow \gamma^*/Z\ g$ annihilation process [4–7], pQCD in LO predicts that the angular coefficients A_0 and A_2 are equal, independent of Parton Distribution Functions (PDFs), or y, and are described by $A_0^{q\bar{q}} = A_2^{q\bar{q}} = \frac{P_T^2}{M_{\ell\ell}^2+P_T^2}$.

For the $qg \rightarrow \gamma^*/Z\ q$ Compton process, A_0 and A_2 depend on PDFs and y. However, in pQCD at LO, when averaged over y, A_0 and A_2 are approximately [8, 9] described by $A_0^{qg} = A_2^{qg} \approx \frac{5P_T^2}{M_{\ell\ell}^2+5P_T^2}$.

The equality $A_2 = A_0$ is known as the Lam-Tung relation [10]. At LO, it is valid for both $q\bar{q}$ and gq processes [5]. Fixed order perturbative QCD calculations [1] in next to leading order (NLO),

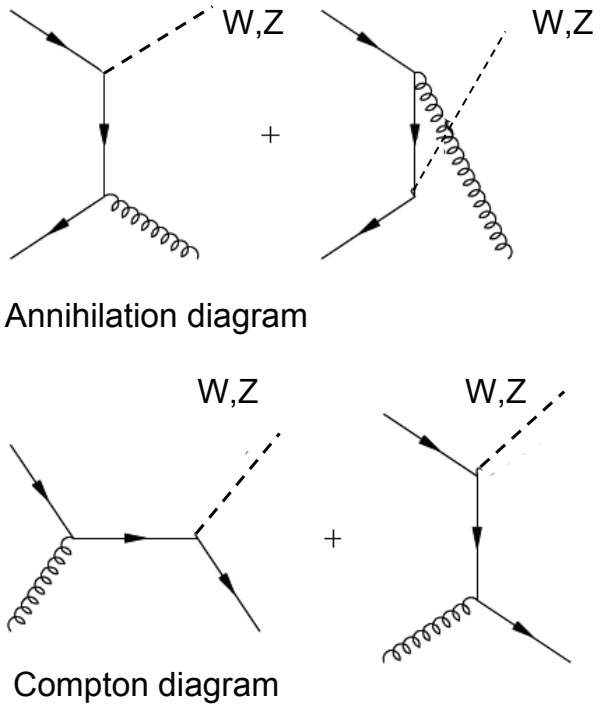

Figure 1: Leading order annihilation ($q\bar{q} \rightarrow \gamma^*/Z\ g$) and Compton ($qg \rightarrow \gamma^*/Z\ q$) diagrams for the production of Z bosons with finite transverse momentum

as well as QCD resummation calculations [6] to all orders indicate that violations of the Lam-Tung relation are small. The Lam-Tung relation is only valid for vector (spin 1) gluons. It is badly broken for scalar (spin 0) gluons [11]. Therefore, confirmation of the Lam-Tung relation is a fundamental test of the vector gluon nature of QCD and is equivalent to a measurement of the spin of the gluon.

Early tests of the Lam-Tung relations were done at fixed target experiments using samples of low mass Drell-Yan dilepton pairs at relatively low transverse momentum. In this region, non-perturbative higher twist effects can be significant. Some experiments report large violations [12–15], and one experiment is consistent [8] with the Lam-Tung relation.

CDF has confirmed that Lam-Tung relationship for Z boson events and published the result at [16]. They also presented the first measurements of the Z boson production angular coefficients at the Tevatron. Here we can test of the Lam-Tung relation at the LHC.

Fixed order pQCD calculations [1] and Monte Carlo generators in next to leading order (NLO) (e.g. Dyrad [17] and MadGraph [18], and the stand alone version [19] of PYTHIA (Z+1jet)) indicate that there is a significant contribution of the Compton process to the production of Z bosons with large transverse momentum at the Tevatron and the LHC. Therefore, these calculations yield values of A_0 and A_2 which are larger than pure annihilation process prediction $\frac{P_T^2}{M_{\ell\ell}^2+P_T^2}$. Similar results are predicted by POWHEG [20], a NLO Monte Carlo with additional parton showering, and FEWZ [21] which is a next to NLO (NNLO) QCD calculation. POWHEG predicts that the A_0 and A_2 at the LHC should be larger than at the Tevatron.

In contrast, the default version of PYTHIA [22], VBP [23], and Monte Carlo generator based on

QCD resummation predict values of A_0 and A_2 which are close to $\frac{P_T^2}{M_{\ell\ell}^2+P_T^2}$ (expected if the $q\bar{q}$ process is dominant). At the Tevatron, the ResBos [24] Monte Carlo generator, which is also based on QCD resummation, predicts values of A_0 and A_2 which are close to $\frac{P_T^2}{M_{\ell\ell}^2+P_T^2}$ at low P_T, and larger values (close to the predictions of fixed order pQCD) at high P_T. Therefore, measurements of A_0 and A_2 as a function of P_T probe the mechanism of production of gauge boson in hadronic collisions.

CDF has done the first measurement of the angular coefficients A_0, A_2, A_3 and A_4, in the Z boson mass region ($66 < M_{ee} < 116$ GeV/c^2) produced at $\sqrt{s} = 1.96$ TeV using the data set which corresponds to an integrated luminosity of 2.1 fb^{-1}. The CDF results show good agreement with the predictions of QCD fixed order perturbation theory (e.g. $POWHEG$) which implies that there is a significant contribution from the Compton process at large P_T. [16] In addition, they find that Lam-Tung relation $A_0 = A_2$ is satisfied.

In this analysis, we measure the angular coefficients using 2-dimensional fitting method which measures full angular coefficients from A_0 to A_7 in terms of the trnasverse momentum (P_T) and rapidity (y). The measured angular coefficients, A_0, A_2, A_3, and A_4, are confirmed by 1 dimentinal fitting method integrating over $\cos\theta$, or ϕ.

2 CMS detector

The CMS detector is a super-conducting solenoid of 6 m internal diameter with a magnetic field of 3.8 T. The detector consists of a silicon pixel and string tracker, a crystal electromagnetic calorimeter (ECAL), and a brass/scintillator hadron calorimeter (HCAL). The inner tracker measures charged particle trajectories in the range of pseudorapidity, $|\eta| < 2.5$, and meaures a transverse-momentum (p_T) with a resolution of $1-2\%$ level for charged particles up to $p_T =$ 100 GeV. The pseudorapidity (η) is defined as $\eta = -ln(tan(\theta/2))$, where θ is the polar angle with respect to the anticlockwise beam direction. In CMS detector, muons are detected using drift tubes, cathode strip chambers, and resistive plate chambers. The muon coverage in the detector is up to $|\eta| < 2.4$ and matching segments from the muon system to tracks measures the muon momentum with a resolution of 1 % to 5 % depending on η region. A more detailed description of CMS detector can be found in [25].

3 Data set and Event selection

The analysis is performed using the full data sample collected at $\sqrt{s}$ = 7 TeV (2011) which corresponds to 4.9 fb^{-1} of the integrated luminosity. We use the double muon trigger sample which has asymmetric p_T threshold, HLT_Mu17_Mu8, to select dimuon candidates. To clean up the sample, the muon selection criteria is required and this selection is defined as a tight muon selection in CMS muon POG recommendation.

Specifically, the selection criteria are following :

- HLT Mu17_Mu8 (available after run = 165970)
- muon p_T >25 GeV and detector $|\eta| < 2.4$
- Muon selection : Tight muon selection is applied
- Global and Tracker Muon
- Global muon normalized fit $\chi^2 < 10$
- Number of Tracker hits greater than 10

- At least one muon chamber hit included in the global-muon track fit
- Number o f pixel hits greater than or equal to 1
- Number of muon stations greater than or equal to 2
- $dxy < 0.2$
- Fractional tracker isolation ($TrkIso_{\Delta R<0.3}/P_T < 0.1$) is applied to at least one leg of two muons
- Mass and rapidity selection : $80 < M_{\mu^+\mu^-} < 100\ GeV/c^2$ and $|y| < 2.4$
- Select di-muon pairs from events with only one di-muon candidate (Event fraction which has more than one di-muon pairs is less than 0.008%)

In the analysis, we restrict the kinematic range, $80 < M_{\mu^+\mu^-} < 100\ GeV/c^2$ and $|y| < 2.4$. Since we apply the loose isolation requirement to avoid any bias of the isolation efficiency in the angular distribution, the tighter muon pt and mass cut is applied to reduce the background contamination in the sample. In the event selection, we reject the events which have the multiple Z candidates which has a negligible effect. (the event fraction which has multiple Z cadidates in the event is less than 0.008%.) After all event selection, we find $\sim$ 1.78 M Z candidates.

The data sample used for the analysis is produced in CMSSW 4_2_x version. The produced data has the detector mis-alignment bias which affects the muon momentum. We applied the muon momentum correction (Rochester correction) in data and MC, which improves the determination of the muon momentum and reduces its dependence on the muon charge, η, and ϕ. More details of the muon momentum correction will be discussed later. For MC, we use *POWHEG* Monte Carlo sample which has Pythia parton showering. The MC sample is also produced CMSSW 4_2_x version (Fall11-PU_S6_START42). Table 1 summarizes the data and MC sample used for the analysis.

Table 1: The data and MC sample used for the analysis.

Data	
Path	Integrated luminosity
/DoubleMu/Run2011A	2.04 fb^{-1}
/DoubleMu/Run2011B	2.86 fb^{-1}
Total luminosity	4.90 fb^{-1}
MC	
Powheg simulation with Pythia parton showering for 7 TeV (30M)	

4 Analysis procedure

The analysis is done in seven bins of transverse momentum (P_T bins : (0,10), (10,20), (20,35), (35,55), (55,80), (80,120), and (120,200)) for two rapidity bins ($|y| < 1.0$ and $1.0 \leq |y| < 2.4$). PDFs and the dilution effect changes in the rapidity, so the measurement in $|y|$ provides better understanding of the mechanism.

The determination of the detector acceptance require that the various kinematic distribution in the MC agree with the data. Specifically, these include the rapidity distributions and the transverse momentum distributions. In general, weighting factors to correct the kinematic distribution in MC are extracted from the ratio of data to MC in the reconstructed level. The weighting factors are then applied to the MC to ensure that the various kinematic distributions in the weighted MC are the same as in data. Since Powheg prediction doesn't describe data well

for Z P_T distribution, an additional tuning for Z P_T distribution is required. The reconstructed Z P_T distribution is compared between data and MC and its ratio is used as the correction factor. The correction factor is applied to MC as the event weighting in the generated Z P_T distribution. The procedure is iterated until the ratio of data to MC is flat. Figure 2 shows the correction factor for Z P_T distribution. After applying Z P_T correction shown in Figure 2, we also refine any possible rapidity dependence ($\sim$ 2%). The data-driven Z P_T correction factor is compared with the correction factor derived from MadGraph and the difference is assigned as a systematic uncertainty for Z P_T modeling.

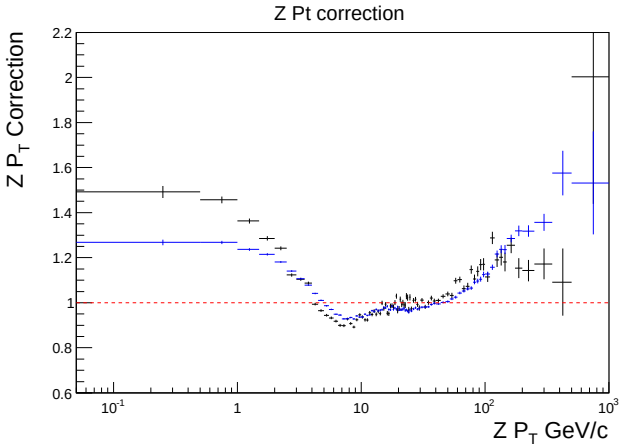

Figure 2: Z P_T correction factor. The black points are the correction factor derived by the data-driven method and the blue points are the correction derived by MadGraph prediction. The difference between the data-driven correction vs. MadGraph correction is assigned as a systematic uncertainty of Z P_T modeling.

4.1 Muon Momentum Scale : Rochester correction

A muon momentum correction [26] is applied to compensate for misalignment of the CMS detector. The primary cause of bias in the reconstructed momentum is the misalignment of the tracker. The tracker geometry is not well modeled in both data and MC and the bias is different between data and MC.

To remove the bias, the muon momentum correction is extracted using the average of $1/p_T$ (i.e. $< 1/p_T >$) spectra of muons from Z decays in the bins of muon charge (Q), θ, and ϕ. On top of $< 1/p_T >$ correction, we extract the additional correction factors using the average of Z mass, $< M^Z_{\mu\mu} >$, in η and ϕ bin of μ^+ or μ^-. The Z mass is less sensitive to the efficiencies, background, and modeling of kinematic distributions. Therefore, the additional correction using Z mass reduces the systematic uncertainty of the correction. This additional correction from Z mass is also propagated into $< 1/p_T >$ correction at the end.

Before the muon momentum correction, the ϕ distribution of Z bosons in the Collins-Soper Frame showed unphysical features that indicated a a bias in reconstruction of positive and negative muons. And this bias is slightly different between the first $2fb^{-1}$ data and the second $2.1fb^{-1}$ data. Therefore, the muon momentum correction is derived for each data set, respectively. After the application of the momentum corrections to the data and MC, it removes the bias from a misalignment and also an possible error in the integral of B*dL.

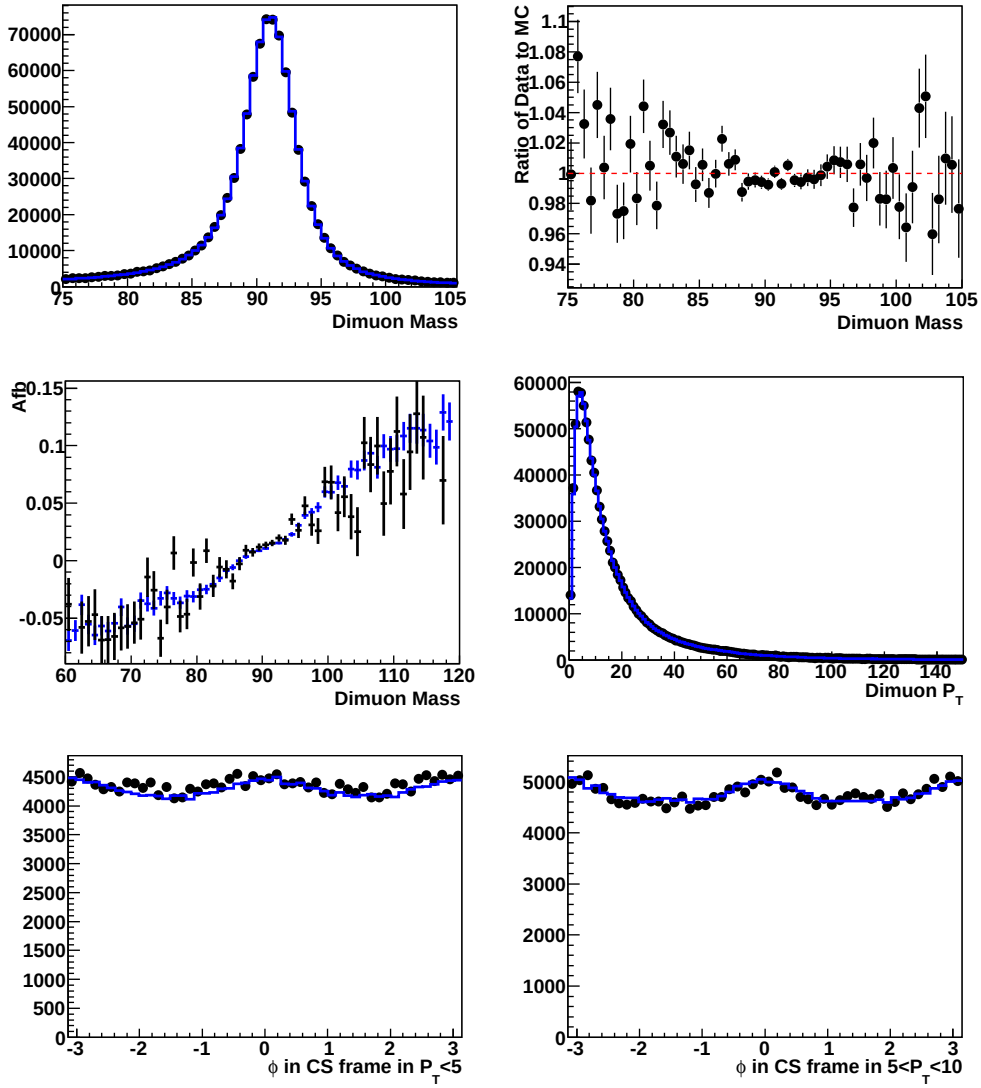

Figure 3: The first reference plot of the muon momentun correction after the correction in the first $2fb^{-1}$ data : Z mass, A_{FB}, Z P_T, and ϕ in Collins-soper frame in low Z P_T. The plots in the first row show the dimuon distribution in data (black) and MC (blue) and its ratio. The plot in the left side of the second row shows the forward-backward asymmetry and the plot in the right side shows Z P_T distribution. The Z P_T distribution in MC is tuned to match the data. The plots in the bottom show ϕ distribution in Collins-soper frame in Z $P_T < 5$ (left) , $5 < Z$ $P_T < 10$ GeV/c (right). The black points corresponds to data and the blue to MC.

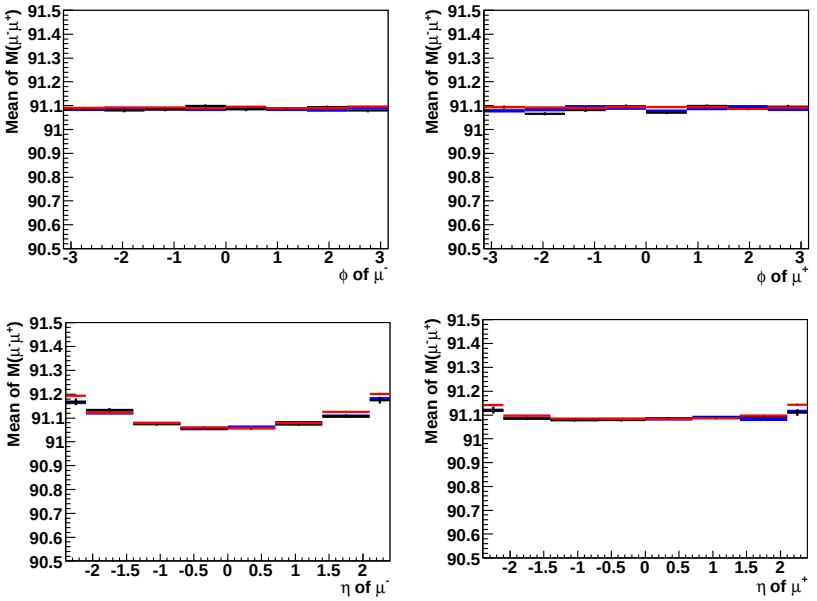

Figure 4: The second reference plot of the muon momentum correction after correction in the first $2fb^{-1}$ data : Z mass profile in muon ϕ and η. The plots in top show the Z mass profile in ϕ of μ^- (left) and μ^+ (right) and the plots in bottom show the Z mass profile in η of μ^- (left) and μ^+ (right). The Z mass corresponds to the average of Z mass in the range of $86.5 < M(\mu\mu) < 96.5$ GeV/c^2. The black points are data, the blue points are MC, and the red points are the generated level after QED radiation which is used as the reference point.

4.2 Efficiencies

4.2.1 Trigger Efficiency

The double muon trigger sample passed HLT_Mu17_Mu8 is used to select di-muon candidates. This trigger path only requires muon p_T threshold, so the trigger efficiency is relatively high in high muon p_T events ($p_T > 20$ GeV) decaying from Drell-Yan process. The trigger efficiency (ϵ^{μ}_{trig}) for each trigger filter, $Mu17$ or $Mu8$, is measured using the tag-and-probe method, respectively. To reduce the background contamination in sample, we apply all muon ID cuts on both the tagged and probe legs. To minimize the trigger bias, SingleMu trigger sample (HLT_IsoMu24) is used to measure the trigger efficiency. The trigger match for HLT_IsoMu24 is required for the tagged leg and the probe leg is used to measure the trigger efficiency. The high pile-up data (2011B) has a lower trigger efficiency, so we measure the trigger efficiency for 2011A and 2011B data separately.

The trigger efficiency is relatively flat as a function of muon p_T for $p_T > 25$ GeV/c, but may have a small η and ϕ dependence. Therefore, the trigger efficiency for the single muon object is measured in terms of muon η and ϕ using the tag and probe method.

For dimuon events, either of two muons needs to pass HLT_Mu8 and another should pass HLT_Mu17. We measure the trigger efficiency of HLT_Mu8 (ϵ^{μ}_{trig8}) and HLT_Mu17 on top of HLT_Mu8 requirement ($\epsilon^{\mu}_{trig17|8}$) and propagate the trigger efficiency of the event ($\epsilon^{2\mu}_{trig}$) following :

$$\epsilon^{2\mu}_{trig} = \epsilon^{\mu}_{trig8}(\eta_1,\phi_1) \times \epsilon^{\mu}_{trig8}(\eta_2,\phi_2) \times (1.0 - (1.0 - \epsilon^{\mu}_{trig17|8}(\eta_1,\phi_1)) \times (1.0 - \epsilon^{\mu}_{trig17|8}(\eta_2,\phi_2))). \quad (3)$$

The trigger efficiency of the event is calculated using the event weighting and Figure 5 shows the trigger efficiency as a function of the angular distributions. The trigger efficiency is relatively flat in the angular distributions.

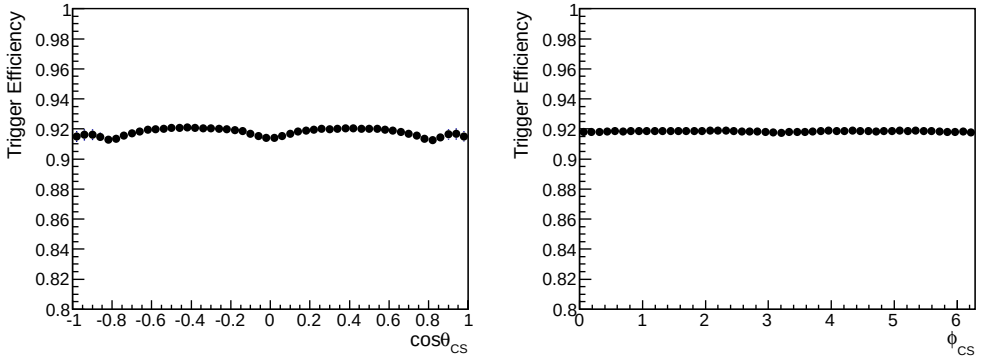

Figure 5: The trigger efficiency as a function of angular distributions, $\cos\theta_{CS}$ and ϕ_{CS}. The left plot shows the trigger efficiency as a function of $\cos\theta$ in Collins-soper frame and the right plot shows the trigger efficiency as a function of ϕ in Collins-soper frame.

4.2.2 Muon Reconstruction Efficiency

We need to make sure that the muon selection efficiency is correctly described in the MC. This is accomplished by applying scale factors to the efficiency in the Monte Carlo to make sure that they match the data. The muon identification selection described in section 3 is applied to select the muon object and remove backgrounds. The muon reconstruction efficiency is measured using the tag-and-probe method as a function of muon η and ϕ as defined in the trigger efficiency. The tagged and probe leg is randomized based on muon p_T to reduce the bias, so on average, the p_T spectrum of both tag and probe legs is the same.

The muon reconstruction efficiency is parameterized to

$$\epsilon_{recon} = \epsilon_{tracking} \times \epsilon_{global} \times \epsilon_{ID} \times \epsilon_{iso} \tag{4}$$

The tagged leg is required to pass all muon ID selection to clean up the sample and also to be matched to the triggered object to remove trigger bias when measuring the muon reconstruction efficiency from the data.

The tracking efficiency is $\sim$ 100 % and the scale factor of data to MC is close to 1.0, so the tracking efficiency is excluded in the parameterization of the muon reconstruction efficiency. A general track is used as a probe to measure the global muon reconstruction efficiency. For the ID efficiency, a global muon is used as a probe and required to pass the tight muon selection criteria described in Section 3.

For the isolation cut, we found that the efficiency of the isolation drops in case of an event around $\pi_{CS} \approx n \times \pi$ (n=0,1,2) in high Z P_T. In this case, two muons decay back-to-back and one muon has a large p_T whereas another muon has small p_T. To balance P_T of the muon pair, the jet goes to the same direction as the low p_T muon and it affects the inefficiency of the isolation of the low p_T muon. To avoid the inefficiency of the isolation in the angular distributions, we apply the loose isolation cut which requires the fractional track isolation ($Iso_{track}/p_T < 0.1$) to at least one muon of two. The isolation cut efficiency is also measured in the same way of

muon ID efficiency and extract the efficiency scale factor in muon η and ϕ. The scale factor of the isolation efficiency for one muon object is 1.0 within the statistical uncertainty.

In the measurement of the muon reconstruction efficiency, the probe leg is required to pass the kinematic selection ($P_T > 20$ GeV/c and $|\eta| < 2.4$) and the efficiency is defined following :

$$\epsilon(\eta, \phi) = \frac{N_{pass}(\eta, \phi)}{(N_{pass}(\eta, \phi) + N_{fail}(\eta, \phi))} \tag{5}$$

Here, N_{pass} is the number of events passing the selection for the probe leg, and N_{fail} is the number of events failed the selection for the probe leg. The background is estimated using the Z mass fitting method. The convolution of Briet-Wigner and Gaussian function is used as the signal and the exponential function is used as the background shape. The mass window, $60 < M_{\mu\mu} < 120$ GeV/c^2 is used for the efficiency study. The efficiency scale factor in η and ϕ is implemented into MC by using event weights.

Figure 6 shows the reconstrction efficiency of events as a function of $\cos\theta_{CS}$ and ϕ_{CS} for low or high Z P_T region. The efficiency is relatively flat after loosening the isolation cut. (The isolation efficiency of having both muons with the fractional isolation < 0.1 goes down to $\sim 80\%$ at $\phi_{CS} = n \times \pi$ for high Z P_T bins.)

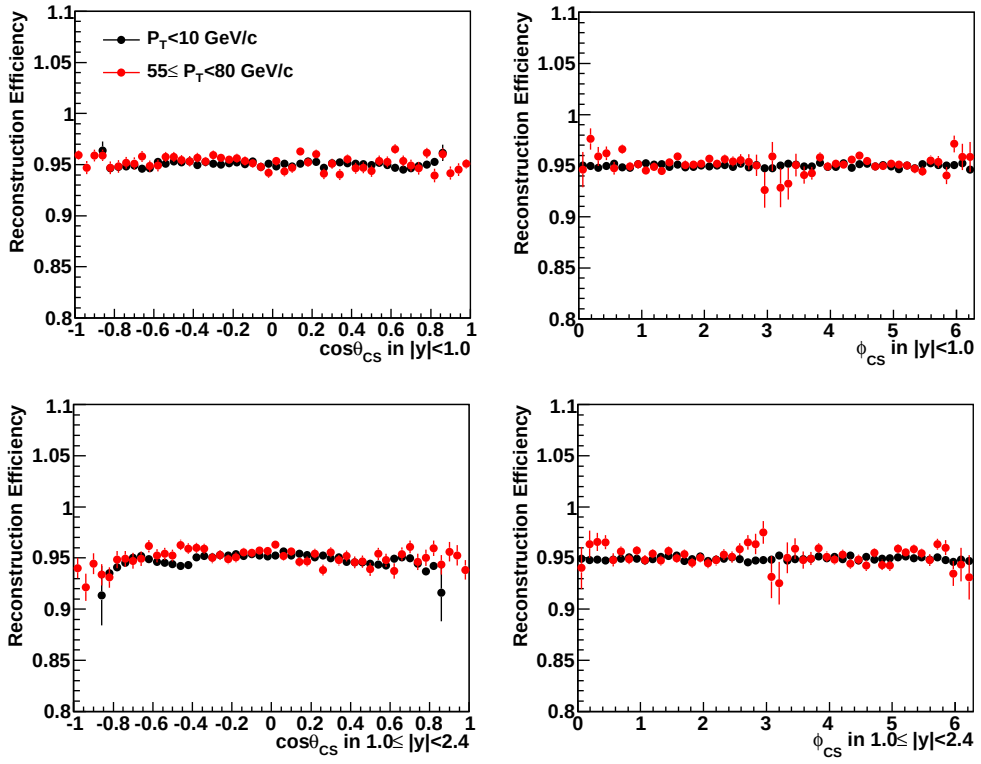

Figure 6: The reconstruction efficiency as a function of the angular distributions for low or high Z P_T bin. The black points correspond to $P_T < 10$ GeV/c and the red points correspond to $55 \leq P_T < 80$ GeV/c.

After applying the corrections, we compare the kinematic distributions of Z boson between data and MC. Figures 7 and 8 show a comparison of various kinematic distributions between the data and MC before the background subtraction.

In the top part of Figure 7 we show a comparison of the invariant mass (left) and boson rapidity (right) distributions between the data (black) and MC (blue). In the bottom part we show a comparison of the boson P_T (left) and NVertices (right) distributions between the data (black) and MC (blue).

In Figure 8 we show a comparison of the $\cos\theta$ (left) and ϕ (right) distributions in the Collins-Soper frame between the data (black) and MC (blue) used for the angular coefficients measurement.

There is a good agreement between data and MC for the various kinematic distributions of the events.

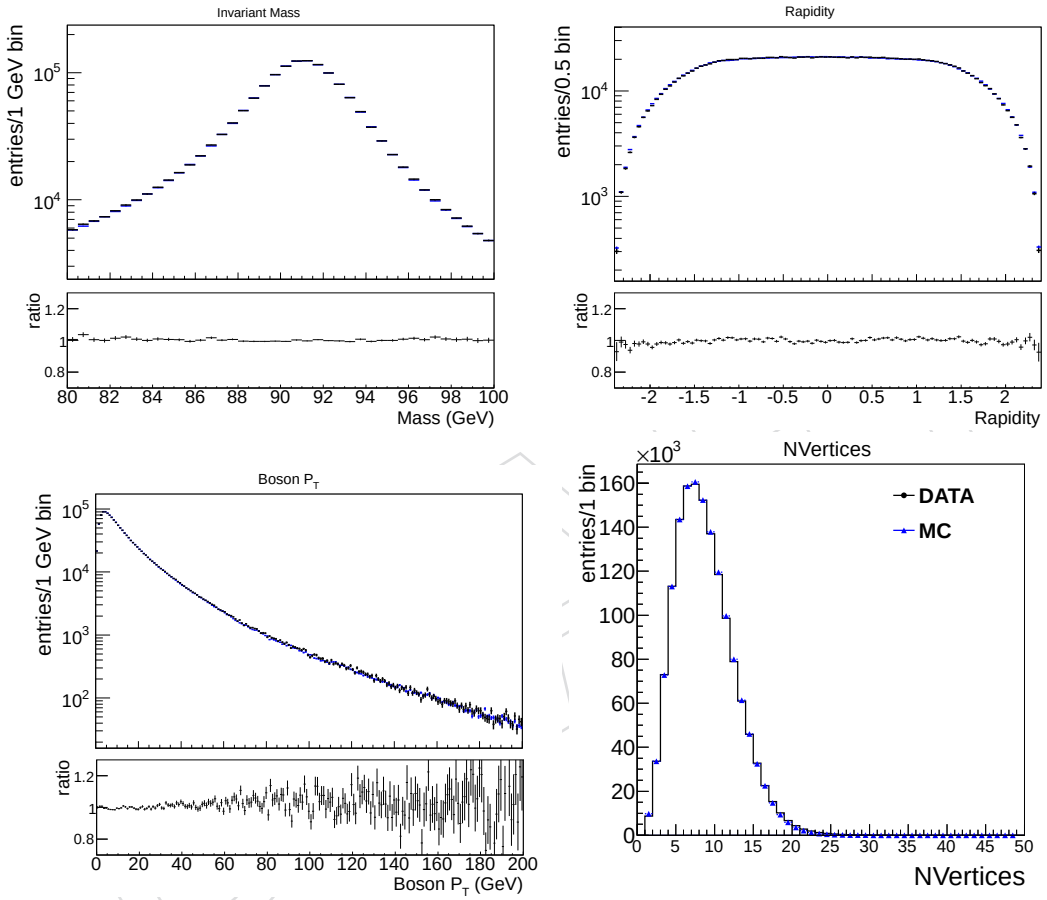

Figure 7: Top Plots: Comparison of the invariant mass (left) and boson rapidity (right) distributions between the data (black) and MC (blue). Bottom plots: Comparison of boson P_T (left) and the number of Z vertices (right) distributions between the data (black) and MC (blue).

4.3 Background Estimation

The dominant backgrounds which pass the selection cuts come from $t\bar{t}$, $\gamma^*/Z \rightarrow \tau\tau$, and diboson ($WW$, WZ, ZZ) production, while tW, single W, and QCD are smaller background processes. We use the data-driven $e\mu$ method to estimate these backgrounds.

The data-driven $e\mu$ background estimation process is possible due to the fact that many of the background processes which decay to two muons in the final state can also decay to an electron and muon in the final state.

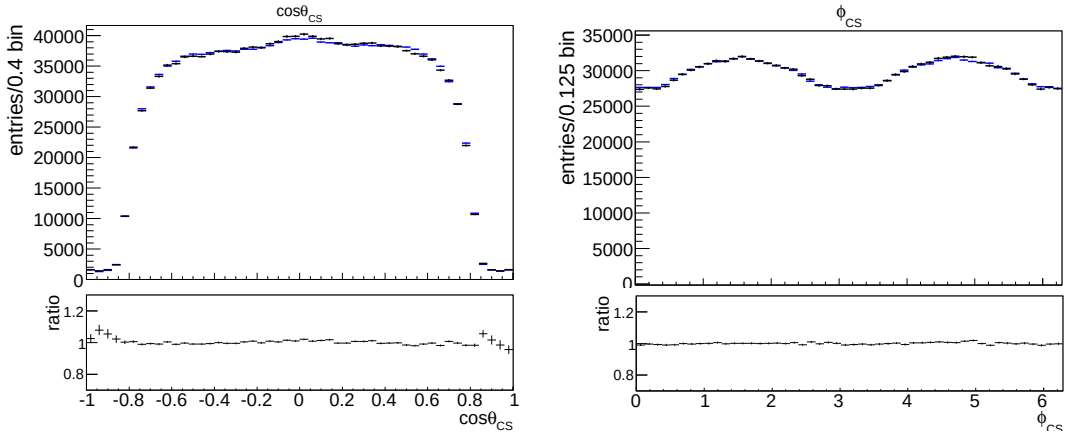

Figure 8: Comparison of the $\cos\theta$ (left) and ϕ (right) distributions in the Collins-Soper frame between the data (black) and MC (blue).

Using MC, we can get the ratio of a background process (such as $t\bar{t}$) to decay to $\mu\mu$ or $e\mu$ in the final state. We assume this ratio to be some constant

$$\frac{t\bar{t} \to \mu\mu}{t\bar{t} \to e\mu} = Constant. \tag{6}$$

This constant should be the same in data as in MC, such that

$$\frac{t\bar{t}_{data} \to \mu\mu}{t\bar{t}_{data} \to e\mu} = Constant = \frac{t\bar{t}_{MC} \to \mu\mu}{t\bar{t}_{MC} \to e\mu}. \tag{7}$$

Rearranging this equation shows that we can estimate the number of $\mu\mu$ background events which come from $t\bar{t}$ events in our sample:

$$t\bar{t}_{data} \to \mu\mu = \frac{t\bar{t}_{MC} \to \mu\mu}{t\bar{t}_{MC} \to e\mu}(t\bar{t}_{data} \to e\mu). \tag{8}$$

We use this $e\mu$ method to estimate all EWK backgrounds except WZ and ZZ processes. The $e\mu$ method cannot cover all possible combination of WZ and ZZ process (only partially measured), so we use the simulations to measure WZ and ZZ background. One benefit of using this method is that many systematic divide out when the $e\mu$ to $\mu\mu$ ratio is taken, so that the data-driven method often has smaller total uncertainties than a pure-MC background.

It is not pratical to generate sufficient MC QCD samples to calculate the QCD background using the $e\mu$ method. We exclude QCD MC when we make the same-sign dilepton distributions and assume that the difference between the data and MC distributions comes from the missing QCD events. We have performed MC studies showing that the majority of QCD events which pass our selection cuts come from b-quarks. Assuming all the missing same-sign QCD events come from b-quarks, we can calculate the number of expected opposite-sign $e\mu$ and $\mu\mu$ pairs and add those to the background sample. This method accounts for all EWK and QCD background processes. We show the final MC and data-driven background estimates in Figure 9. Two methods have a good agreement each other, but data-driven method has more fluctuations. Therefore, the simulation method is used to estimate the background, which provides the smoother angular distributions.

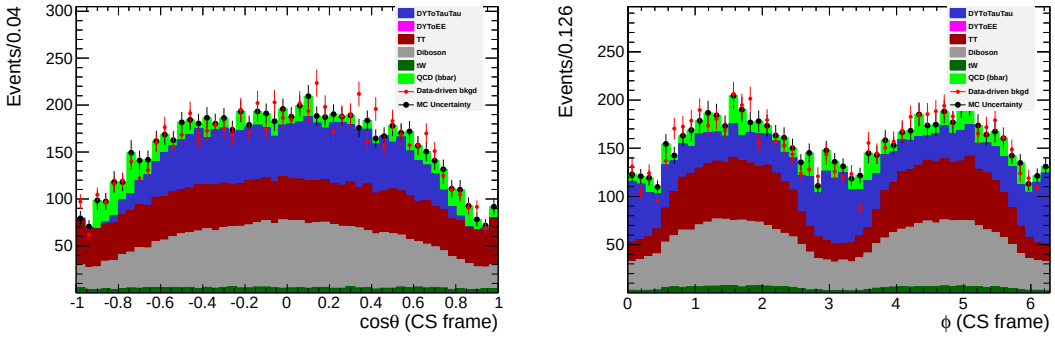

Figure 9: MC and data-driven backgrounds of $\cos\theta$ and ϕ in the Colins-Soper frame.

4.4 Extraction of Angular coefficients

4.4.1 2-dimensional fitting method

We assume that the observed CMS angular distribution factors into the acceptance and the underlying distribution as

$$\frac{d\sigma}{d\Omega} = A(\cos\theta,\phi)s(\cos\theta,\phi) + A(\cos\theta,\phi)b(\cos\theta,\phi) \tag{9}$$

where $A(\cos\theta,\phi)$ is the acceptance, $w(\cos\theta,\phi)$ is the angular distribution containing all angular coefficients ($A_0 - A_7$), and $B(\cos\theta,\phi)$ is the background distribution. We perform a χ^2 fit in each transverse momentum range to extract all eight angular coefficients which give the best overall fit to the observed data distribution. We fit the background distribution $b(\cos\theta,\phi)$ with the general angular distribution expression for a spin-1 particle with an extra $\cos^4\theta$ term. 2-dimensional fitting method performed the fit for $\cos\theta$ and ϕ at the same time, so it take account of any possible correlation between $\cos\theta$ and ϕ distributions.

4.4.2 1-dimensional fitting method

As described above in Equation 1 and 3, $\cos\theta_{CS}$ is determined by A_0 and A_4 integrating over ϕ_{CS} and ϕ_{CS} is determined by A_2 and A_3 asumming A_5 and A_7 are zero. Fitting each $\cos\theta_{CS}$ or ϕ_{CS} distribution in binned of Z boson rapidity and P_T extracts A_0 and A_4 from $\cos\theta_{CS}$ and A_2 and A_3 from ϕ_{CS} distribution.

To extract A_0 and A_4, data and *POWHEG* Monte Carlo simulated events are binned in $\cos\theta$ for each transverse momentum range. The Monte Carlo (MC) events are re-weighted to generate the expected experimental distributions for a range of values of A_0 and A_4. A maximum likelihood comparison of the data and Monte Carlo distributions in $\cos\theta$ is used to extract the best values of the angular coefficients A_0 and A_4 that describe the data.

Similarly, for each transverse momentum range, data and Monte Carlo simulated events are also binned in ϕ. A maximum likelihood comparison of the data and Monte Carlo distributions in ϕ is used to extract the best values of the angular coefficients A_2 and A_3 that describe the data. 1-dimensional fitting method integrates over $\cos\theta$ or ϕ to measure (A_0,A_4) or (A_2,A_3) coefficients. Therefore, this method have more statistic power to measure each combination than 2-dimensional fitting method. In addition, 1-dimensional fitting method was used for CDF measurement. Therefore, the result from 1-dimensional fitting method is useful to compare with CDF meas urement.

4.5 Systematic uncertainty

In this section, we summarize the systematic uncertainty sources considered in the measurement. We consider the systematic uncertainty contribution from the efficiency measurement, the muon momentum correction, the background estimation, the pile-up correction, the modeling of Z P_T distribution, QED final state radiation (FSR) modeling, and PDFs.

The muon reconstruction efficiency is estimated using the tag and probe method as a function of η and ϕ and the signal yield is extracted from Z mass fitting method ($60 < M_{\mu^+\mu^-} < 120$ GeV/c^2). This efficiency is also measured using the event counting method in the tight mass window, $80 < M_{\mu^+\mu^-} < 100$ GeV/c^2, to reduce the background contamination. The efficiency deviation between the fitting method vs. the event counting method is assigned as a systematic uncertainty of the efficiency measurement. To assign the systematic uncertainty from the efficiency in the angular coefficients measurement, we smear the efficiency scale factor by 1 sigma of the total error and run toy MC samples varying the efficiency scale factor. The RMS of the deviation from toy MC tests is assigned as a systematic uncertainty for the muon reconstruction efficiency. In addition, we also consider η and p_T dependent efficiency and estimate the effect in the measurement compared to η and ϕ dependent efficiency. The η and p_T dependent efficiency affects mostly A_0 and A_2 in low Z P_T region.

For the systematic uncertainty of the muon momentum correction, we also use the same approach used for the systematic uncertainty of the efficiency. The muon momentum correction has its own uncertainty of the measurement and the central value of the muon momentum correction is smeared by 1 sigma of the total error in each toy MC sample. The RMS of the deviation from the central value in the angular coefficients from toy MC tests is assigned as a systematic uncertainty for the muon momentum correction.

The background estimation has $\sim$ 30 % of systematic uncertainty overall. We vary the background with $\pm$ 1 sigma of total error (stat. $\oplus$ syst.) as a function of $\cos\theta_{CS}$ and ϕ_{CS} and estimate the deviation of the angular coefficients. The deviation from the central value is assigned as a systematic uncertainty of the background estimation.

Since MC is generated in low pile-up scenario, the pile-up correction is applied to MC to match to the data. The pile-up distribution measured in the data has $\sim$ 5% level of the systematic uncertainty. Therefore, we vary the pile-up distribution of the data by $\pm$ 5 % and recalculate the pile-up correction of data to MC. This recalculated pile-up correction is applied in MC and extracted the angular coefficients using this re-weighted MC sample. We compare the difference between the central value and the re-extracted angular coefficients with $\pm$ 5% changes and the deviation is assigned as a systematic uncertainty for the pile-up correction.

Z P_T distribution in POWHEG MC doesn't describe the data well. We derived the Z P_T correction using the data-driven method and the measured correction is applied to MC. This data-driven Z P_T correction is compared with the high order QCD prediction, MadGraph, which is shown in Figure 2. To assign the systematic uncertainty for Z P_T modeling, we measure the angular coefficients with MadGraph Z P_T correction and estimate the deviation of the angular coefficients measured with the data-driven Z P_T correction.

For QED final state radiation (FSR), we rely on POWHEG FSR modeling in the measurement. To estimate the systematic uncertainty of FSR modeling, we applied FSR reweighing factor developed using a parton-shower approach (Pythia) and assign the difference with FSR reweighing in the angular coefficients measurement as a systematic uncertainty.

POWHEG MC sample uses CT10 PDFs as a default. To assign the systematic uncertainty of

PDFs modeling, we consider CT10, MSTW2008nlo, and NNPDF2.0 PDFs set with 68% CL variation. The deviation from various PDFs weighting is considered to assign the systematic uncertainty of PDFs. For 1-dimensional fitting method, PDFs uncertainty includes the uncertainty from CT10 and MSTW2008nlo PDFs sets and 2-dimensional fitting methods considers MSTW2008nlo and NNPDF2.0 PDFs. (We will synchronize PDFs uncertainty before pre-approval.)

Figure 10 shows the component of systematic error in each coefficients. In the systematic uncertainty, PDFs uncertainty, the muon momentum correction, and (η,p_T) dependent efficiency are the leading sources.

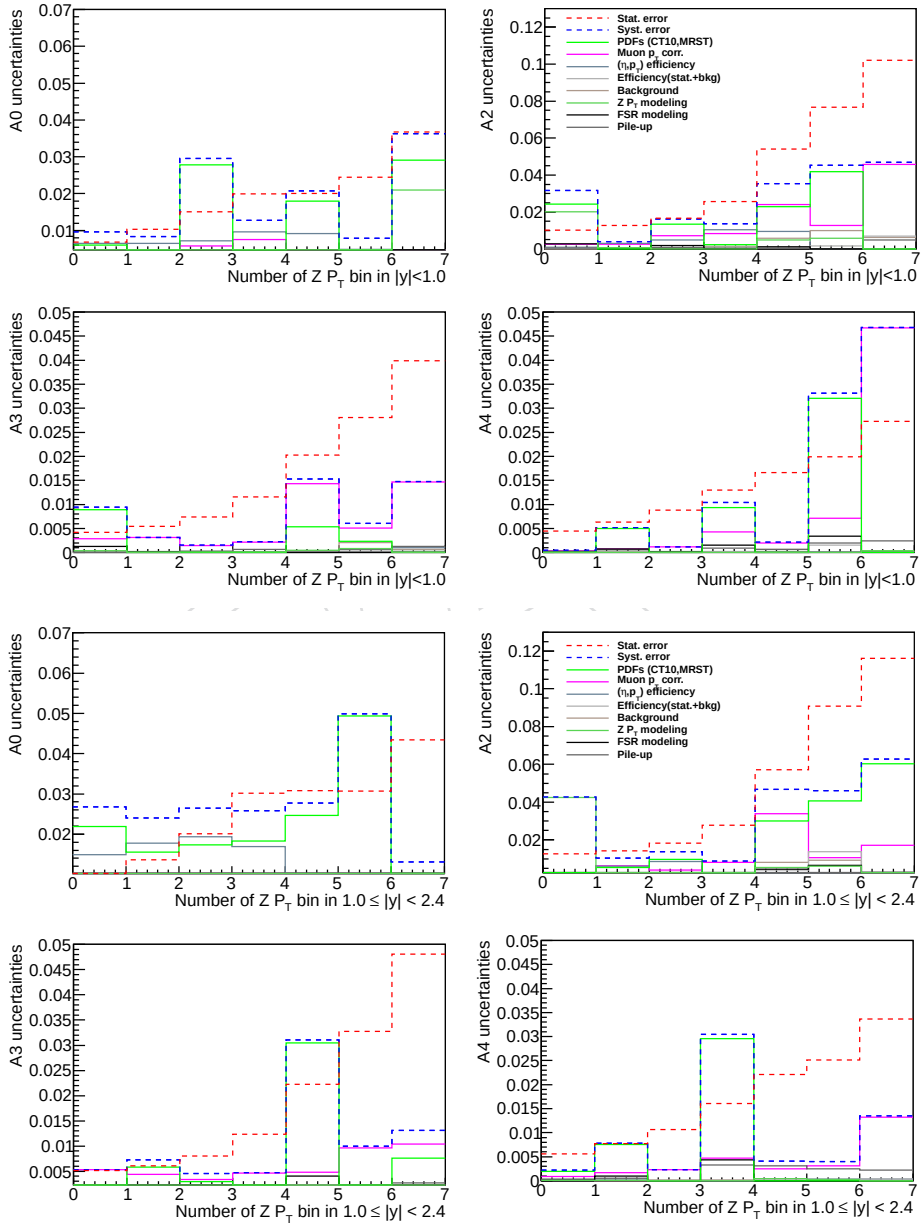

Figure 10: Uncertainty component in angular coefficients. Top four plots are for $|y| < 1.0$ and bottom four plots are for $1.0 \leq |y| < 2.4$. The x-axis corresponds to the number of Z P_T bin.

4.6 Result

The results for A_0, A_2, A_3, and A_4 are shown in Figure 11 and 12 with full statisical and systematic uncertainties. Results are dominated by statistical uncertainty with PDF uncertainty being the next largest contributor. Results from the two different fitting methods have reasonable agreement with each other. Some bins, especially at A_2, shows roughly 1 simga deviation and we find that this difference comes from the way of the background subtraction. 1-dimensional fitting method uses bin-by-bin subtraction, whereas 2-dimensional method smoothes out the background distribution and then normalized the area by the total background yield. The difference of background subtraction affects more in high P_T region where the statistics is lower , but the background contamination is higher. We will improve the way of the background subtraction for better consistent result later.

A_0 and A_2 tend to increase with Z P_T as expected within the predicted limits for $q\bar{q}$ and qg production though A_2 values deviate from POWHEG predictions as Z P_T increases, most notably in the higher rapidity bin. We test any possible sources to affect the measurement in the analysis like the remaining muon momentum bias, any charge dependent efficiency, and background. However, none of these don't affect the result. A_2 in high y region tends to agree with ResBos prediction, but ResBos has lower A_0 than POWHEG and obey Lam-Tung relation ($A_0 = A_2$). Therefore, A_0 has large deviation from ResBos prediction. The averaged $A_0 - A_2$ in 1-dimensional fitting method is 0.0645 ± 0.0138 for $|y| < 1.0$ and 0.0562 ± 0.0196 for $1.0 \leq |y| < 2.4$. Therefore, the data doesn't allow Lam-Tung relation which has the different result from CDF measurement. The values for A_3 are consistent with zero as predicted by theory. Values for A_4 are also consistent between the two methods and consistent with POWHEG predictions within uncertainties.

Results of the fit for A_1 are shown in Figure 13 for the 2D fitting method only since the 1D fitting method cannot observe A_1. There is generally good agreement between the fit results with POWHEG, with better agreement at lower Zy. Results for A_5, A_6, and A_7 are not shown here but are consistent with zero as predicted by theory.

The 2-dimensional fitting result are also summarized in Table 2 and 3.

References

[1] E. Mirkes and J. Ohnemus *Phys. Rev. D* **50, 51** (1994, 1995) 5692, 4891.

[2] J. C. Collins and D. E. Soper *Phys. Rev. D* **16** (1977) 2219.

[3] "The coordinates in the laboratory frame are (θ,ϕ,z), where θ is the polar angle relative to the direction of one of the proton beams(the $+z$ axis), and ϕ the azimuth. The pseudorapidity is $\eta = -ln\ tan(\theta/2)$. For an $\mu^+ + \mu^-$ pair $P_T = Psin\theta$, $E_T = Esin\theta$, and $y = \frac{1}{2} ln \frac{E+P_z}{E-P_z}$, where P and P_z are the magnitude and z component of the momentum, and E is the energy of the $\mu^+ + \mu^-$ pair",.

[4] J. C. Collins *Phys. Rev. Lett.* **42** (1979) 291.

[5] D. Boer and W. Vogelsang *Phys. Rev. D.* **74** (2006) 014004.

[6] E. L. Berger, J.-W. Qiu, and R. A. Rodriguez-Pedraza *Phys. Lett. B.* **656** (2007) 74.

[7] A. Bodek *Eur.Phys.J. C* **67** (2010) 321.

[8] L. Y. Z. et al. *Phys. Rev. Lett.* **99** (2007) 082301.

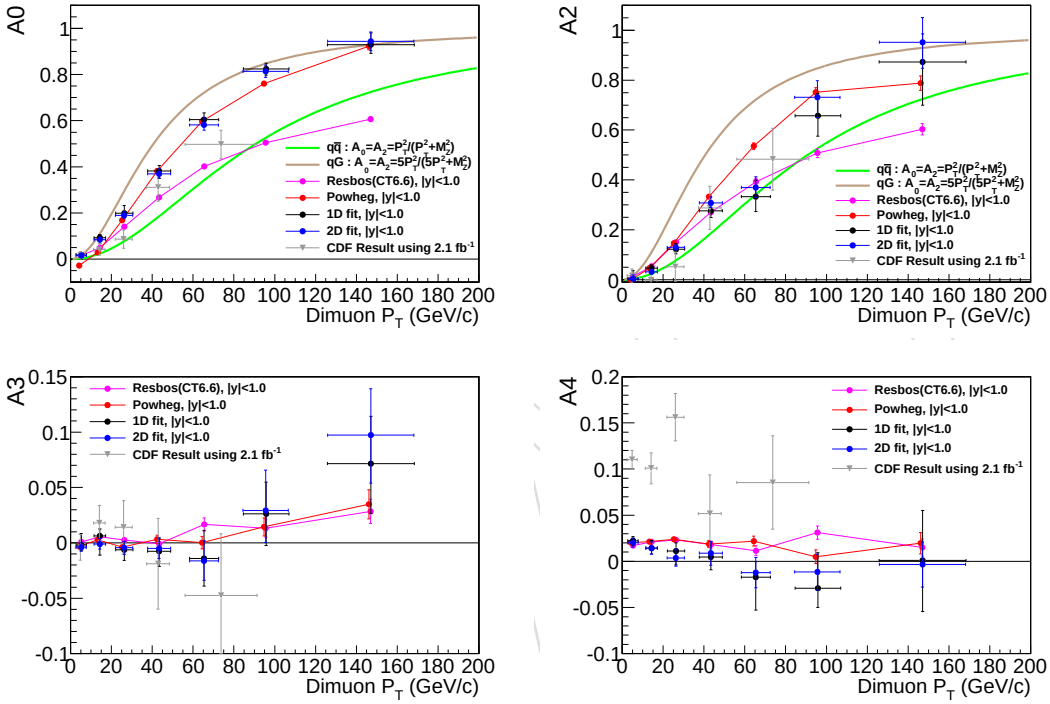

Figure 11: Comparison of the CMS measured values of A_0, A_2, A_3 and A_4 (shown with full statistical and systematic uncertainties) for $|Zy| < 1.0$ with the 1D and 2D fitting methods and POWHEG and ResBos predictions. Results of the two different methods have agreement within uncertainties. Results disagree with A_2 POWHEG predictions as $Z_P T$ increases. CDF measurement corresponds to full rapidity range in $66 < M < 116$ GeV range.

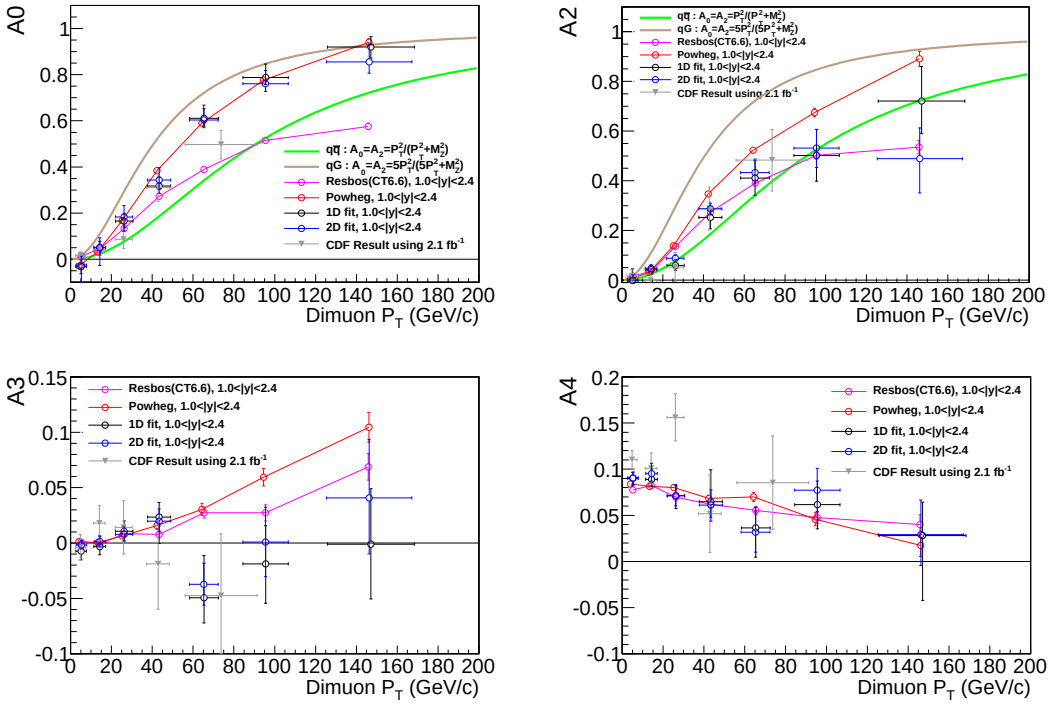

Figure 12: Comparison of the CMS measured values of A_0, A_2, A_3 and A_4 (shown with full statistical and systematic uncertainties) for $1.0 < |Zy| < 2.4$ with the 1D and 2D fitting methods and POWHEG predictions. Results of the two different methods have agreement within uncertainties. Results disagree with A_2 POWHEG predictions as Z_PT increases.CDF measurement corresponds to full rapidity range in $66 < M < 116$ GeV range.

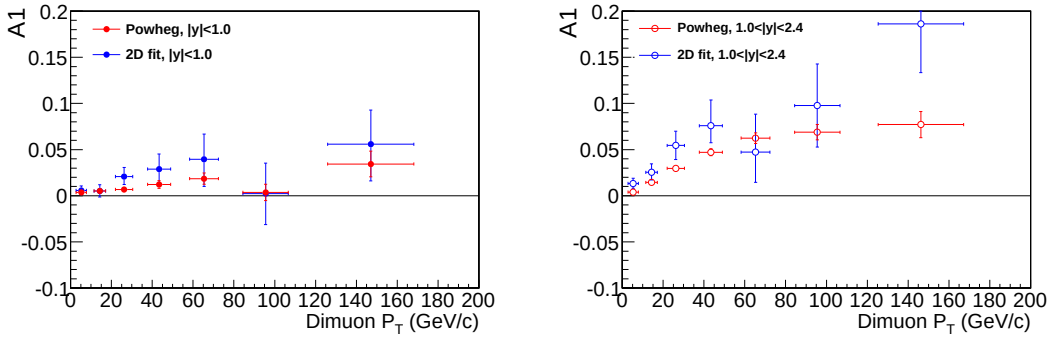

Figure 13: Comparison of the CMS measured values of A_1 (shown with full statistical and systematic uncertainties) for $|Zy|$ <1. (left) and $1.0 < |Zy| < 2.4$ (right) between the 1D fitting method and POWHEG predictions.

γ^*/ZP_T	0–10	10–20	20–35	35–55	55–80	80–120	120–200	200–400
A0	0.0162	0.0843	0.1897	0.3699	0.5817	0.8136	0.9442	0.9942
Stat. error	± 0.0061	± 0.0092	± 0.0128	± 0.0169	± 0.0197	± 0.0259	± 0.0390	± 0.0808
Syst. error	$\pm^{0.0079}_{0.0088}$	$\pm^{0.0080}_{0.0043}$	$\pm^{0.0096}_{0.0076}$	$\pm^{0.0151}_{0.0045}$	$\pm^{0.0248}_{0.0073}$	$\pm^{0.0067}_{0.0036}$	$\pm^{0.0086}_{0.0123}$	$\pm^{0.0280}_{0.0347}$
Total error	$\pm^{0.0100}_{0.0107}$	$\pm^{0.0122}_{0.0101}$	$\pm^{0.0160}_{0.0149}$	$\pm^{0.0227}_{0.0175}$	$\pm^{0.0316}_{0.0210}$	$\pm^{0.0268}_{0.0262}$	$\pm^{0.0400}_{0.0409}$	$\pm^{0.0855}_{0.0879}$
A1	0.0057	0.0051	0.0208	0.0289	0.0395	0.0023	0.0559	0.0966
Stat. error	± 0.0040	± 0.0057	± 0.0084	± 0.0151	± 0.0267	± 0.0327	± 0.0368	± 0.0786
Syst. error	$\pm^{0.0027}_{0.0023}$	$\pm^{0.0038}_{0.0028}$	$\pm^{0.0053}_{0.0023}$	$\pm^{0.0062}_{0.0017}$	$\pm^{0.0060}_{0.0122}$	$\pm^{0.0051}_{0.0068}$	$\pm^{0.0043}_{0.0147}$	$\pm^{0.0091}_{0.0179}$
Total error	$\pm^{0.0048}_{0.0046}$	$\pm^{0.0068}_{0.0063}$	$\pm^{0.0099}_{0.0087}$	$\pm^{0.0164}_{0.0152}$	$\pm^{0.0274}_{0.0294}$	$\pm^{0.0331}_{0.0334}$	$\pm^{0.0371}_{0.0396}$	$\pm^{0.0792}_{0.0806}$
A2	0.0041	0.0313	0.1294	0.3082	0.3697	0.7310	0.9522	1.0130
Stat. error	± 0.0065	± 0.0089	± 0.0118	± 0.0183	± 0.0373	± 0.0666	± 0.0970	± 0.1675
Syst. error	$\pm^{0.0135}_{0.0025}$	$\pm^{0.0085}_{0.0030}$	$\pm^{0.0043}_{0.0021}$	$\pm^{0.0145}_{0.0042}$	$\pm^{0.0216}_{0.0120}$	$\pm^{0.0082}_{0.0452}$	$\pm^{0.0169}_{0.0354}$	$\pm^{0.0810}_{0.0428}$
Total error	$\pm^{0.0149}_{0.0070}$	$\pm^{0.0123}_{0.0094}$	$\pm^{0.0125}_{0.0120}$	$\pm^{0.0233}_{0.0188}$	$\pm^{0.0431}_{0.0392}$	$\pm^{0.0671}_{0.0805}$	$\pm^{0.0984}_{0.1033}$	$\pm^{0.1861}_{0.1729}$
A3	-0.0039	-0.0011	-0.0044	-0.0049	-0.0162	0.0293	0.0972	0.0394
Stat. error	± 0.0030	± 0.0041	± 0.0056	± 0.0091	± 0.0176	± 0.0284	± 0.0417	± 0.0904
Syst. error	$\pm^{0.0024}_{0.0023}$	$\pm^{0.0029}_{0.0018}$	$\pm^{0.0014}_{0.0021}$	$\pm^{0.0019}_{0.0018}$	$\pm^{0.0045}_{0.0018}$	$\pm^{0.0227}_{0.0040}$	$\pm^{0.0041}_{0.0116}$	$\pm^{0.0173}_{0.0353}$
Total error	$\pm^{0.0039}_{0.0038}$	$\pm^{0.0050}_{0.0045}$	$\pm^{0.0058}_{0.0060}$	$\pm^{0.0093}_{0.0092}$	$\pm^{0.0181}_{0.0177}$	$\pm^{0.0363}_{0.0287}$	$\pm^{0.0419}_{0.0433}$	$\pm^{0.0920}_{0.0970}$
A4	0.0202	0.0143	0.0036	0.0088	-0.0122	-0.0114	-0.0034	0.0310
Stat. error	± 0.0044	± 0.0063	± 0.0087	± 0.0126	± 0.0162	± 0.0190	± 0.0242	± 0.0549
Syst. error	$\pm^{0.0023}_{0.0018}$	$\pm^{0.0021}_{0.0012}$	$\pm^{0.0042}_{0.0011}$	$\pm^{0.0019}_{0.0039}$	$\pm^{0.0011}_{0.0039}$	$\pm^{0.0016}_{0.0052}$	$\pm^{0.0023}_{0.0039}$	$\pm^{0.0185}_{0.0093}$
Total error	$\pm^{0.0050}_{0.0047}$	$\pm^{0.0066}_{0.0064}$	$\pm^{0.0096}_{0.0087}$	$\pm^{0.0127}_{0.0132}$	$\pm^{0.0162}_{0.0166}$	$\pm^{0.0191}_{0.0197}$	$\pm^{0.0243}_{0.0245}$	$\pm^{0.0579}_{0.0557}$

Table 2: Angular coefficients result with the uncertainty measured by 2D fit result for $|y| < 1.0$

[9] J. Lindfors *Physica Scripta* **20** (1979) 19.

[10] C. S. Lam and W. K. Tung *Phys. Lett. B* **80** (1979) 228.

[11] N. N. N. Arteaga-Romero and J. Silva *Phys. Rev. Lett.* **52** (1984) 52.

[12] S. F. et al. *Z. Phys. C* **31** (1986) 513.

[13] M. G. et al. *Z. Phys. C* **37** (1988) 545.

[14] J. S. C. et al. *Phys. Rev. D* **39** (1989) 92.

[15] J. G. H. et al. *Phys. Rev. D* **44** (1991) 1991.

[16] CDF Collaboration *Phys. Rev. Lett.* **106** (2011) 241801.

[17] W. Giele, E. Glover, and D. A. Kosower *Nucl. Phys. B* **403** (1993) 633.

[18] F. Maltoni and T. Stelzer *JHEP* **0302** (2003) 027.

[19] T. S. et al. *JHEP* **05** (2006) 026.

[20] S. A. et al. *arXiv:1009.5594v1* (2010).

[21] K. Melnikov and F. Petriello *Phys. Rev. Lett.* **96** (2006) 231803.

[22] T. S. et al. *JHEP* **05** (2006) 026.

[23] R. K. Ellis and S. Veseli *Nucl. Phys. B* **511** (1998) 649.

γ^*/ZP_T	0–10	10–20	20–35	35–55	55–80	80–120	120–200	200–400
A0	-0.0250	0.0508	0.1836	0.3432	0.6035	0.7611	0.8559	0.9300
Stat. error	± 0.0076	± 0.0111	± 0.0159	± 0.0223	± 0.0268	± 0.0318	± 0.0491	± 0.1278
Syst. error	$\pm^{0.0373}_{0.0959}$	$\pm^{0.0410}_{0.0768}$	$\pm^{0.0471}_{0.0591}$	$\pm^{0.0484}_{0.0348}$	$\pm^{0.0585}_{0.0160}$	$\pm^{0.0474}_{0.0090}$	$\pm^{0.0600}_{0.0052}$	$\pm^{0.1289}_{0.3921}$
Total error	$\pm^{0.0381}_{0.0962}$	$\pm^{0.0425}_{0.0776}$	$\pm^{0.0497}_{0.0612}$	$\pm^{0.0533}_{0.0413}$	$\pm^{0.0643}_{0.0312}$	$\pm^{0.0571}_{0.0331}$	$\pm^{0.0776}_{0.0494}$	$\pm^{0.1815}_{0.4124}$
A1	0.0133	0.0254	0.0546	0.0759	0.0473	0.0977	0.1862	0.0549
Stat. error	± 0.0047	± 0.0066	± 0.0096	± 0.0172	± 0.0316	± 0.0405	± 0.0486	± 0.1099
Syst. error	$\pm^{0.0030}_{0.0027}$	$\pm^{0.0065}_{0.0049}$	$\pm^{0.0119}_{0.0119}$	$\pm^{0.0218}_{0.0065}$	$\pm^{0.0263}_{0.0085}$	$\pm^{0.0195}_{0.0195}$	$\pm^{0.0407}_{0.0193}$	$\pm^{0.8799}_{0.8062}$
Total error	$\pm^{0.0056}_{0.0054}$	$\pm^{0.0093}_{0.0082}$	$\pm^{0.0153}_{0.0153}$	$\pm^{0.0278}_{0.0184}$	$\pm^{0.0411}_{0.0327}$	$\pm^{0.0449}_{0.0449}$	$\pm^{0.0634}_{0.0523}$	$\pm^{0.8868}_{0.8136}$
A2	-0.0022	0.0475	0.0878	0.2867	0.4325	0.5310	0.4886	0.6064
Stat. error	± 0.0066	± 0.0091	± 0.0122	± 0.0187	± 0.0382	± 0.0723	± 0.1217	± 0.2896
Syst. error	$\pm^{0.0222}_{0.0029}$	$\pm^{0.0108}_{0.0056}$	$\pm^{0.0052}_{0.0022}$	$\pm^{0.0148}_{0.0074}$	$\pm^{0.0290}_{0.0209}$	$\pm^{0.0195}_{0.0278}$	$\pm^{0.0235}_{0.0651}$	$\pm^{0.1287}_{0.3987}$
Total error	$\pm^{0.0231}_{0.0072}$	$\pm^{0.0141}_{0.0106}$	$\pm^{0.0133}_{0.0124}$	$\pm^{0.0239}_{0.0201}$	$\pm^{0.0480}_{0.0436}$	$\pm^{0.0749}_{0.0774}$	$\pm^{0.1240}_{0.1381}$	$\pm^{0.3169}_{0.4928}$
A3	-0.0017	0.0013	0.0078	0.0198	-0.0373	0.0009	0.0407	0.1630
Stat. error	± 0.0031	± 0.0042	± 0.0058	± 0.0094	± 0.0186	± 0.0308	± 0.0491	± 0.1184
Syst. error	$\pm^{0.0025}_{0.0023}$	$\pm^{0.0027}_{0.0019}$	$\pm^{0.0034}_{0.0015}$	$\pm^{0.0055}_{0.0016}$	$\pm^{0.0042}_{0.0030}$	$\pm^{0.0064}_{0.0044}$	$\pm^{0.0193}_{0.0106}$	$\pm^{0.6702}_{0.6002}$
Total error	$\pm^{0.0040}_{0.0038}$	$\pm^{0.0050}_{0.0046}$	$\pm^{0.0068}_{0.0060}$	$\pm^{0.0109}_{0.0095}$	$\pm^{0.0190}_{0.0188}$	$\pm^{0.0314}_{0.0311}$	$\pm^{0.0528}_{0.0503}$	$\pm^{0.6805}_{0.6117}$
A4	0.0905	0.0953	0.0711	0.0611	0.0318	0.0773	0.0290	0.0107
Stat. error	± 0.0055	± 0.0077	± 0.0106	± 0.0157	± 0.0212	± 0.0233	± 0.0323	± 0.0788
Syst. error	$\pm^{0.0034}_{0.0044}$	$\pm^{0.0081}_{0.0022}$	$\pm^{0.0055}_{0.0017}$	$\pm^{0.0043}_{0.0062}$	$\pm^{0.0058}_{0.0039}$	$\pm^{0.0045}_{0.0028}$	$\pm^{0.0190}_{0.0084}$	$\pm^{0.8051}_{0.0253}$
Total error	$\pm^{0.0065}_{0.0071}$	$\pm^{0.0112}_{0.0081}$	$\pm^{0.0120}_{0.0108}$	$\pm^{0.0163}_{0.0169}$	$\pm^{0.0220}_{0.0215}$	$\pm^{0.0237}_{0.0235}$	$\pm^{0.0375}_{0.0334}$	$\pm^{0.8090}_{0.0828}$

Table 3: Angular coefficients result with the uncertainty measured by 2D fit result for $1.0 \leq |y| < 2.4$.

[24] P. N. F. Landry, R. Brock and C.-P. Yuan *Phys. Rev. D* **67** (2003) 073016.

[25] S. C. et al. (CMS) *JINST* **3** (2008) S08004.

[26] J. H. W. S. Bodek, A. van Dyne and A. Strelnikov *Eur. Phys. J. C* **72** (2012) 72.